

Nanoscale

Accepted Manuscript



This is an *Accepted Manuscript*, which has been through the Royal Society of Chemistry peer review process and has been accepted for publication.

Accepted Manuscripts are published online shortly after acceptance, before technical editing, formatting and proof reading. Using this free service, authors can make their results available to the community, in citable form, before we publish the edited article. We will replace this *Accepted Manuscript* with the edited and formatted *Advance Article* as soon as it is available.

You can find more information about *Accepted Manuscripts* in the [Information for Authors](#).

Please note that technical editing may introduce minor changes to the text and/or graphics, which may alter content. The journal's standard [Terms & Conditions](#) and the [Ethical guidelines](#) still apply. In no event shall the Royal Society of Chemistry be held responsible for any errors or omissions in this *Accepted Manuscript* or any consequences arising from the use of any information it contains.

Cite this: DOI: 10.1039/c0xx00000x

www.rsc.org/xxxxxx

ARTICLE TYPE

Revealing the carbohydrate pattern on the cell surface by super-resolution imaging

Junling Chen,^{a, b} Jing Gao,^{a, b} Jiazhen Wu^{a, b}, Min Zhang^{a, b}, Mingjun Cai,^a Haijiao Xu,^a Junguang Jiang,^a Zhiyuan Tian,^c and Hongda Wang^{* a}

Received (in XXX, XXX) Xth XXXXXXXXX 20XX, Accepted Xth XXXXXXXXX 20XX

DOI: 10.1039/b000000x

Carbohydrates are involved in various physiological and pathological activities, including cell adhesion, signal transduction and tumor invasion. The distribution of carbohydrates is the molecular basis of their multiple functions, but remains poorly understood. Here, we employed direct stochastic optical reconstruction microscopy (dSTORM) to visualize the pattern of N-acetylglucosamine (N-GlcNAc) on Vero cell membranes at nanometer level resolution. We found that N-GlcNAcs exist in irregular clusters on the apical membrane, with the average cluster area at about $0.37 \mu\text{m}^2$. Most of these N-GlcNAc clusters are co-localized with lipid rafts by dual-color dSTORM imaging, suggesting carbohydrates are closely associated with lipid rafts as the functional domains. Our results demonstrate that super-resolution imaging is capable of characterizing the distribution of the cellular surface carbohydrates at the molecular level.

Introduction

Cells are coated with carbohydrates (e.g. glycoproteins and glycolipids), which play a pivotal role in a variety of physiological and pathological activities, including cell adhesion, molecular recognition, signal transduction, endocytosis and immunity.¹⁻³ Variations in cell surface carbohydrates are generally associated with the occurrence of diseases and the metastatic behavior of tumor cells.⁴⁻⁶ However, due to the structural complexity and the difficulty in their synthesis and isolation,⁷ saccharides remain as the least understood class of biomolecules. In the past years, studies of carbohydrates and carbohydrate-protein interactions have been implemented by electrochemical methods,⁸ surface plasmon resonance (SPR),⁹ fluorescence spectroscopy,¹⁰ UV-vis absorption spectroscopy,¹¹ and lectin microarray^{12, 13}. These technologies provide a better understanding of the structure and function of saccharides; additionally, there were a few of the fluorescent imaging of glycans by metabolic labelling,^{14, 15} owing to the low resolution, the detailed distribution of glycans cannot be distinguished. Therefore, more efforts are necessary to reveal the comprehensive information about carbohydrates at the molecular level under native conditions.

Super-resolution imaging techniques¹⁶⁻¹⁸ capable of breaking the diffraction limit of light¹⁹ and achieving lateral resolution of tens of nanometers, such as stimulated emission depletion (STED),^{20, 21} (direct) stochastic optical reconstruction microscopy ((d)STORM),^{22, 23} and (fluorescence) photoactivated localization microscopy ((f)PALM)²⁴⁻²⁶, have been widely implemented in biological research, such as the organization of biomolecules on the cell membrane^{27, 28}. dSTORM²⁸⁻³⁰ uses one kind of organic

dye as photoactivable fluorescent probe to label the target biomolecule. During the imaging process, only a sparse, optically resolvable subset of dyes can be switched into the fluorescent state and then localized and finally turned back into the dark state each time, enabling probes with spatially overlapping images to be separated in time. These cycles are repeated many times so that enough locations are recorded to reconstruct a new image with ultra-high resolution, providing dSTORM a supereminent capability of revealing the nanometer-scale organization of biomolecules on the plasma membrane.

Recently, Markus Sauer *et al.* performed the super-resolution imaging to observe the distribution of three kinds of glycans on SK-N-MC neuroblastoma cells and U2OS cells by metabolic labelling.³¹ According to the related literatures,³² the glycans they imaged with metabolic labelling were the non-native glycans, which may significantly differ from native state of glycans on the cell membrane.

N-acetylglucosamine (N-GlcNAc), as a type of monosaccharide derivative, is a part of the common motif of N-linked sugar chain of transmembrane proteins, including receptors or adhesion molecules. The mutation of N-polysaccharides of cellular receptors will result in cancer invasion and metastasis by altering these receptor functions.^{33, 34}

Here, we applied dSTORM imaging combined with image-based cluster analyses to elucidate how the native N-GlcNAcs distribute on the Vero apical and basal cell membranes, with being labelled with Alexa647-linked WGA. Moreover, we investigated the relationship between the N-GlcNAc clusters and lipid rafts by dual-color dSTORM imaging.

Experimental section

Cell culture

Vero cells, from Shanghai Institute of Biological Sciences, were maintained in a 5% CO₂ environment at 37°C in minimal essential medium (MEM, HyClone), supplemented with 10% fetal bovine serum (FBS, HyClone), 100 U/mL penicillin and 100 µg/mL streptomycin. For dSTORM imaging, Vero cells were cultured on a clean cover slide (22 mm × 22 mm, Fisher) for approximately 24 hours to achieve a ~70% confluence in the same medium.

The sample preparation for dSTORM imaging

The cultured cells were washed 3X with pre-warm PBS, then incubated in 500 µL 4% paraformaldehyde (PFA) (or with 0.2% glutaraldehyde (GA)) in 1× PBS at room temperature for 40 min. After rinsing 3X with PBS, cells were stained with 50 µL Alexa647-conjugated WGA (wheat germ agglutinin) solution (labelling concentration was ~0.1 µM; binding ratio was ~0.5 to 1) at 4°C for 10 min. Then, the excess WGA solution was removed, and cells were washed 4X with PBS. Before imaging, 30 µL imaging buffer (containing 140 mM beta-mercaptoethanol (βME), 0.5 mg/mL glucose oxidase and 40 µg/mL catalase) was dropped on microscope slide (24 mm × 50 mm, Fisher), then the small coverslip where cells were seeded was gently sealed on the large microscope slide by nail polish (Figure S1A-left).

For super-resolution imaging of live cell, cells were washed 3X with pre-warm PBS, then directly stained with Alexa647-conjugated WGA. After that, cells were treated with the same procedures as those for the fixed cells.

For the blocking experiment of 3% BSA (Bovine Serum Albumin), after fixing and washing, we blocked cells with 500 µL 3% BSA for 1 h at 25°C, then washing and staining cells as above.

For the dual-color super-resolution imaging, the fixed cells were labelled with 50 µL lipid raft markers (10 µg/mL, cholera toxin subunit B (recombinant), Alexa Fluor 555 conjugates, Molecular Probes) at room temperature for 20 min, the excess reaction solution was removed; then cells were stained with Alexa647-linked WGA as described above, after being washed 4X with PBS.

Super-resolution dSTORM imaging

dSTORM images were acquired on an inverted Nikon Ti-E microscope with an oil-immersion objective (100×, 1.49 NA, Nikon, Japan), as well as an objective-type TIRF illumination which can significantly decrease the background noise around single molecules. During imaging, a 640 nm laser (~40 mW) was used for both the Alexa647 fluorescent excitation and fluorophore photoswitching. When performing dual-color dSTORM imaging, to avoid the bleaching of Alexa647 by 561 nm laser illumination during imaging lipid rafts, we first imaged N-GlcNAcs with the excitation of 647 nm laser, then imaged lipid rafts by being excited with 561 nm laser. Meanwhile, an excitation filter (ZET405/488/561/647x, 25 mmR, Chroma), a dichroic mirror (ZT405/488/561/647rpc, 25.5 mm × 36 mm × 1 mm, Chroma) and an emission filter set (ZET405/488/561/640m, Chroma) were set in beam path for sample illumination and imaging. Finally, an electron multiplying charge coupled device (EMCCD, Photometrics, Cascade II) camera was required for acquiring

frames (512 × 512 pixels) at high speed, with the pixel size of 160 nm. In our experiments, according to the trend that the GlcNAc cluster changes with the increasing frame number, 5000 frames with 40 ms exposure time were collected to reconstruct a dSTORM image (figure S10). In the course of imaging, we stabilized the sample with two clips to reduce the possibility of x-y drift, and the z-drift was eliminated by a focus lock. Besides, owing to the very short acquisition time, the stage shift can be ignored.

Super-resolution dSTORM images were reconstructed from raw image sequences with the QuickPALM software,³⁵ which is available as a plug-in for ImageJ processing software (U.S. National Institutes of Health). In order to effectively reduce interference from the color crosstalk during dual-color dSTORM imaging, we improved the analysis threshold in QuickPALM, including minimum SNR (signal noise ratio) and maximum FWHM (full width at half maximum), to remove the error points from the color crosstalk as much as possible, as these points were relatively ambiguous and less bright. We controlled the percent of color crosstalk under 8% in dual-color dSTORM imaging with this method, ensuring that the experiment results were credible.

Image-based cluster analyses with ImageJ.

Because the N-GlcNAc clusters on the Vero cellular membranes were large and obvious, it was not necessary to use the Ripley's K analysis to confirm that N-GlcNAcs were distributed in clusters. We directly used the ImageJ to perform image-based cluster analyses. First, with the 'denoise' in ImageJ, the sparse single points were removed from original dSTORM image (Figure S9 A) to make the outlines of clusters clearer (Figure S9 B). Then, the reconstruction image was converted to a binary image by using the 'Analysis Particles' in ImageJ, and the qualified clusters were extracted by setting suitable parameters, such as the area and the circularity of cluster (Figure S9 C). At last, we obtained the useful morphology information of these qualified clusters by setting the measurement in ImageJ, including the area, the circularity, the perimeter, and the Feret's diameter of cluster.

For calculation of the density of clusters per unit area of cellular surface, a square region in the cellular membrane was selected as the region of interest (ROI) to be analyzed with the same cluster analyses method. Then, the total number of the qualified clusters and the total area of the qualified clusters on the ROI were calculated (If some clusters were not automatically recognized, we could manually select them and measure their area).

Results and discussion

Before imaging N-GlcNAcs on cell membranes, the localization precision of single Alexa 647-linked WGA is firstly determined. From Figure S2, multiple WGA clusters containing repeating localizations of the same molecule are aligned by their center of mass to generate a histogram of localizations; then, we fit the histogram to a Gaussian profile to obtain the localization precision of 23.7±1.8 nm. Considering the complicated cellular environment, we also measure that the localization precision on the cell membrane is 25.0±2.7 nm (Figure S3).

By calculating the average densities of localizations on cell

Cite this: DOI: 10.1039/c0xx00000x

www.rsc.org/xxxxxx

ARTICLE TYPE

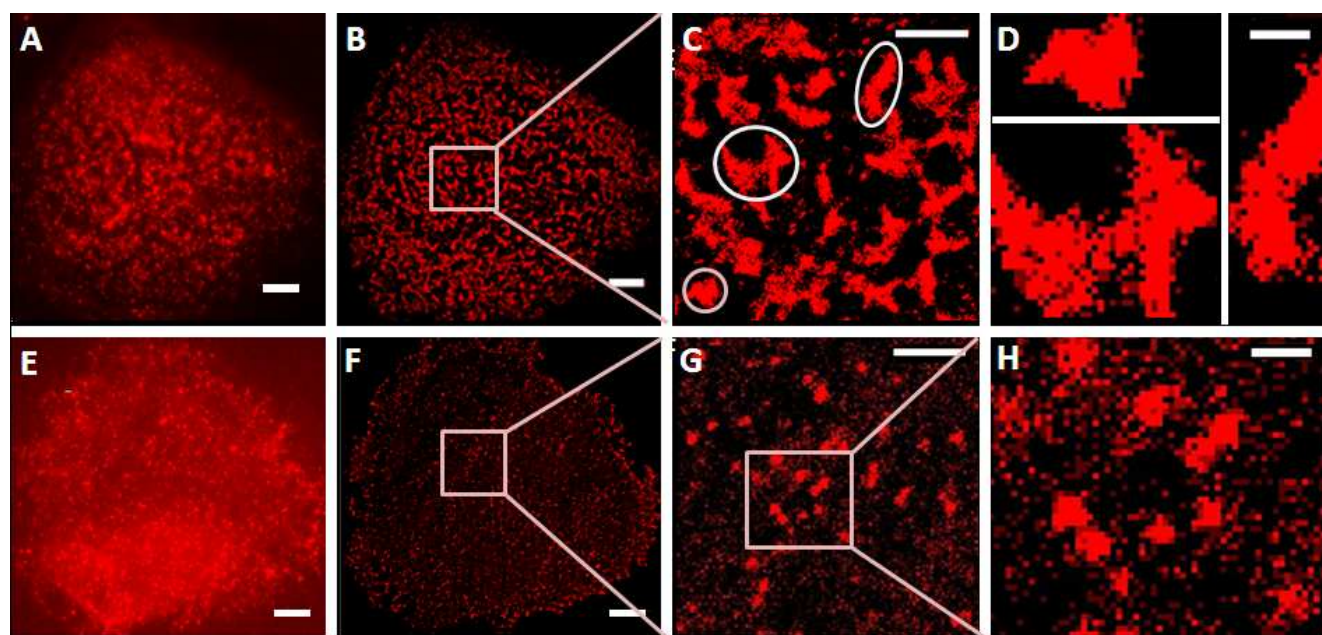


Fig.1. Super-resolution images of N-GlcNAcs on the Vero apical and basal membranes. Compared with blurry conventional TIRF images of N-GlcNAcs on the Vero apical (A) and basal (E) membranes, corresponding dSTORM images (B and F) reveal the distribution features of N-GlcNAcs on cellular membranes at the nanometer resolution. Enlarged images (C and G) illustrate the detailed differences in the distribution of N-GlcNAcs. The further enlarged images show three representative clusters of N-GlcNAcs on the apical surface (D), and almost uniform and small clusters on the basal membrane (H). Scale bars are 5 μm in A, B, E and F. Scale bars are 2 μm in C and G. Scale bars are 200 nm in D and H.

basal and apical membranes at increasing concentration of Alexa647-linked WGA, the saturated labelling concentrations ($\sim 0.1 \mu\text{M}$ for the basal membrane, and $\sim 0.08 \mu\text{M}$ for the apical membrane) were determined to ensure that all N-GlcNAcs in cell membranes were labelled in the imaging experiments (Figure S4, S5).

It is well known that single WGA has two subunits and eight carbohydrate recognition domains (CRD). Taking the lectin-mediated agglutination into account,⁴ we performed a series of the fixation experiments of 4% PFA with different fixation time (Figure S6A, B and C), and found that using 4% PFA to fix cells with 40 min was suitable to effectively avoid the aggregation induced by WGA. As control experiments to rule out the possibility of the artificial clustering caused by WGA, the nanoscale distribution of N-GlcNAcs on the insufficiently fixed apical membrane (Figure S6A) and live Vero apical membranes (Figure S6D) were investigated. Their results remarkably differed from that on the sufficiently fixed cell membranes (Figure S6B, C), providing a clue of the influence from the agglutination of WGA on unfixed cells. Additionally, we also imaged the fixed cells with 4% PFA and 0.2% glutaraldehyde (GA), and found that the result was almost similar as that on the fixation with 4% PFA (Figure S6E).

Besides, we applied the 3D-fluorescent imaging of N-GlcNAcs to confirm that there was no fluorescent molecule in the fixed cell with 40 min (Figure S7).

We also attempted to block the non-specific binding by 3% bovine serum albumin (BSA), and found that non-specific binding has almost no effect on our imaging results (Figure S8).

Comparing with conventional TIRF blurry image of N-GlcNAcs on the Vero apical membrane (Figure 1A), the corresponding dSTORM image shows the substantially improved resolution (Figure 1B). The magnified image (Figure 1C) clearly demonstrates that N-GlcNAcs tend to form the large and dense clusters on the Vero apical membrane. Moreover, these clusters are featured with irregular shapes including ellipse, long strip and irregular polygon (Figure 1D). Interestingly, the organization of N-GlcNAcs on the basal membrane is markedly different from that on the apical membrane by comparing their corresponding dSTORM reconstructed images (Figure 1B, F), rather than the TIRF images (Figure 1A, E). The enlarged images (Figure 1G, H) revealed that most N-GlcNAcs on the basal membrane are sparsely integrated into small and elliptic clusters.

In addition, the superimposed images of TIRF and dSTORM (Figure S11) and the comparison between Deltavision imaging system and dSTORM imaging (Figure S12) further show that the dSTORM imaging with a better resolution is ideal to display the morphology of N-GlcNAc cluster.

To accurately describe the morphological features of N-GlcNAc clusters on the Vero apical and basal membranes, we applied the cluster analyses on the distribution of N-GlcNAcs with a built-in function of Particles Analysis of ImageJ.³⁶ By

Cite this: DOI: 10.1039/c0xx00000x

www.rsc.org/xxxxxx

ARTICLE TYPE

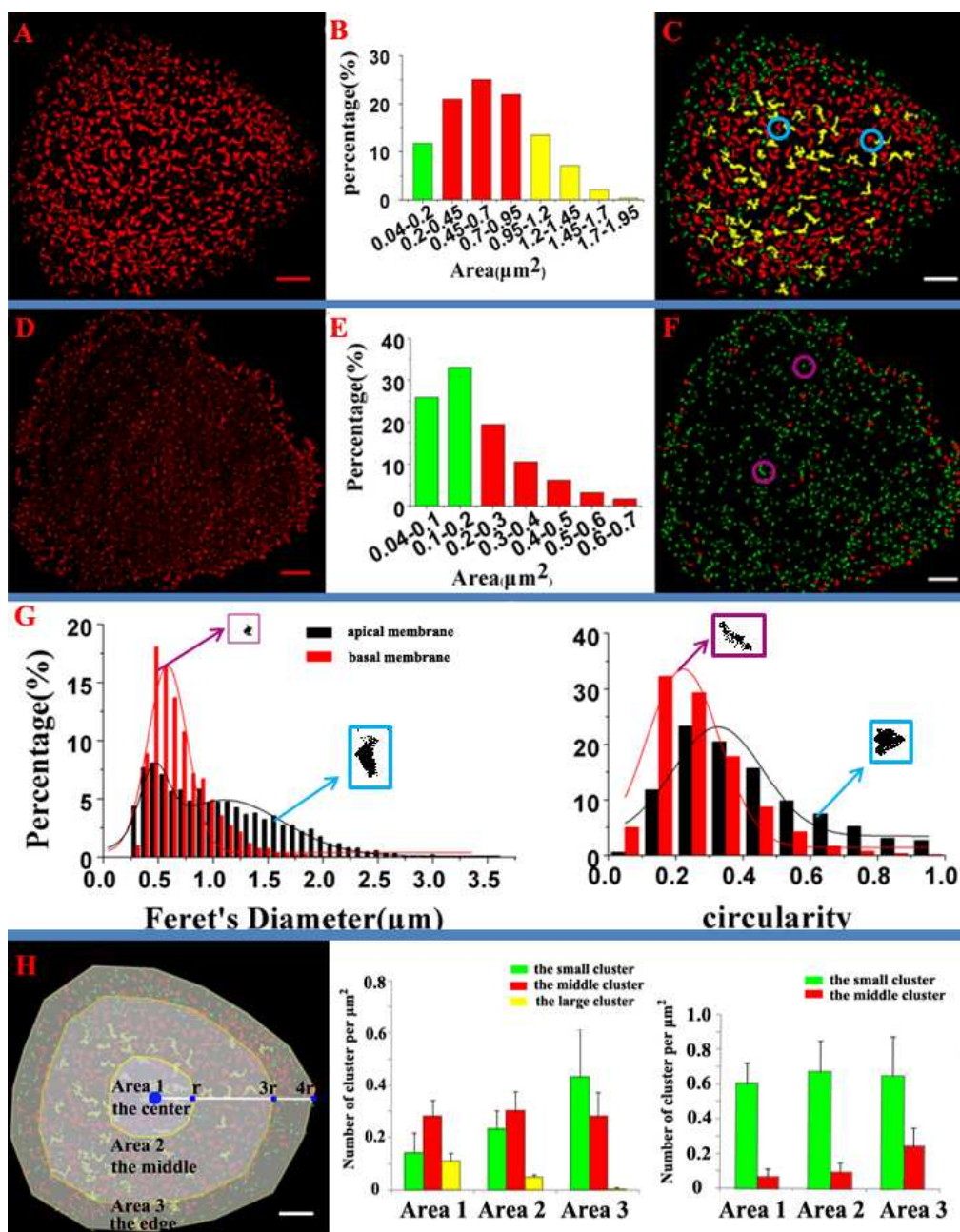


Fig.2. Image-based cluster analyses of the distributions of N-GlcNAc clusters on the Vero apical and basal membranes revealing their distribution patterns. (A and D) dSTORM reconstruction images of N-GlcNAcs on the representative Vero apical and basal membranes. (B and E) Histogram of cluster areas. Green, red and yellow columns indicate the small clusters ($<0.2 \mu\text{m}^2$), the middle clusters ($0.2-0.95 \mu\text{m}^2$) and the large cluster ($>0.95 \mu\text{m}^2$), respectively. These data were analyzed from total qualified clusters on the apical (4865 clusters) and basal membranes (5626 clusters) of ten cells in three repeated experiments. (C and F) dSTORM images with marking the clusters by different colors based on the figure B and figure E, demonstrating their distribution relationship on the apical and basal membranes. (G) Histograms of the Feret's diameters (left) and circularities (right) of total qualified clusters on the apical and basal membrane. The fitting curves show a double peak distribution for the Feret's diameter on the apical membrane (G-left) and a gamma distribution for circularity (G-right). The insets in purple and blue boxes show typical clusters with different Feret's diameters and circularities. (H) with segmenting the cell membrane as three areas (H-left), the statistical analyses of the distribution of the various clusters on the apical (H-middle) and basal membranes (H-right). Scale bars are $5 \mu\text{m}$ in A, C, D, F and H-left.

Cite this: DOI: 10.1039/c0xx00000x

www.rsc.org/xxxxxx

ARTICLE TYPE

setting a threshold of the minimal cluster area ($0.04 \mu\text{m}^2$), the qualified clusters ($>0.04 \mu\text{m}^2$) were extracted from dSTORM image (Figure 2A) for further analysis. According to the area percentages (Figure 2B), all clusters on the apical membrane were sorted to three classes and assigned with three colors to clarify the distribution of various clusters (Figure 2C). 66.2% of clusters ranging from 0.2 to $0.95 \mu\text{m}^2$ were assigned to the middle cluster (the red cluster); the small cluster (0.04 to $0.2 \mu\text{m}^2$, the green cluster) with a small percentage (11.7%) appeared mainly on the edge of membrane; the large cluster ($>0.95 \mu\text{m}^2$, the yellow cluster) preferred to distribute on central membrane. To further illustrate the clusters on the apical membrane, we utilized the semi-quantitative analysis to estimate the average number of N-GlcNAcs per cluster and the density of WGA per unit area of the cell membrane (Figure S13). One third of clusters were the relatively large cluster including more than ten WGAs. Considering that one WGA possesses eight CRDs, it is reasonable to estimate that a typical cluster on the apical membrane might carry tens or hundreds of N-GlcNAcs. Meanwhile, compared the density of WGA on whole cell membrane with that in the cluster, we found almost three quarters

of WGAs band with the N-GlcNAcs in the cluster.

The N-GlcNAc clusters on the Vero basal membrane (Figure 2D) were also analyzed to extract the quantitative information on the morphological features. Based on Figure 2E, ~59% of the qualified clusters ($>0.04 \mu\text{m}^2$) ranging from $0.04 \mu\text{m}^2$ to $0.7 \mu\text{m}^2$ was the small clusters (0.04 - $0.2 \mu\text{m}^2$, green columns), and its proportion increased five folds as compared with the counterpart percentage (~11%) on the apical membrane. Notably, no large cluster was found on the basal membrane, significantly differing from that on the apical surface (Figure 2E). Moreover, the small clusters (green) scattered throughout the basal membrane, and a large number of the middle clusters (red) sparsely distributed at the edge of the basal membrane (Figure 2F).

The distributions of Feret's diameters (Figure 2G-left) and perimeters (Figure 2G-right) of the qualified clusters on the apical (4865 clusters) and basal membranes (5626 clusters) were plotted for detailed morphological features of cluster. The Feret's diameter, a typical physical parameter for particle diameter distributes with double peaks, indicating two main kinds of clusters ranging from 0.269 to $3.581 \mu\text{m}$ distribute on the apical

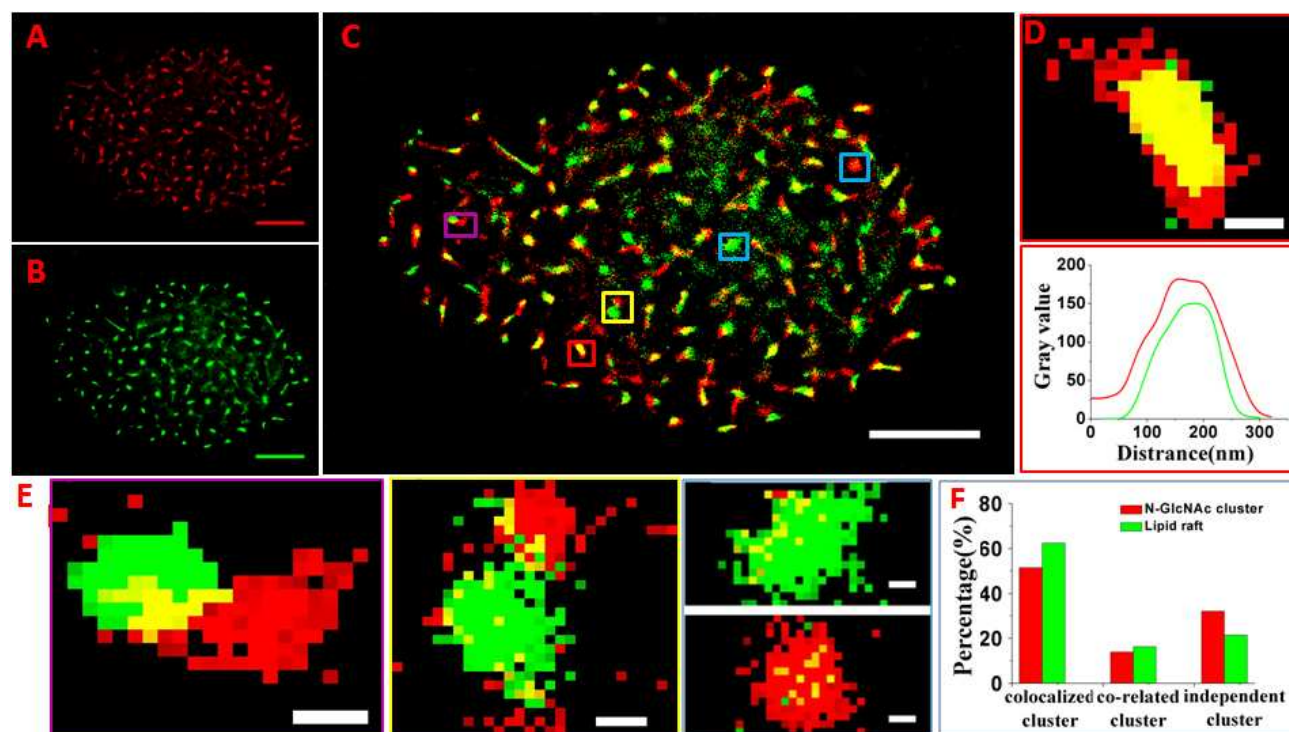


Fig.3. Dual-color dSTORM images revealing the positional relationship between clusters of N-GlcNAcs and lipid-raft domains on the Vero apical membrane. (A) dSTORM image of N-GlcNAcs on the representative Vero apical surface by being labeled with Alexa647-linked WGA. (B) dSTORM image of lipid rafts on the same cellular membrane strained with lipid raft marker. (C) Composite graph of Figure A and B, showing that two types of molecules are mostly co-localized. D-up) Magnified image of the red box region in Figure C, displaying a typical co-localized relationship of two domains. The corresponding intensity profiles of two domains (D-below) also show that they are perfectly co-localized. (E) Enlarged graphs of boxed regions in Figure C classify three kinds of positional relationships, i.e. the co-localized domains whose overlapping area (yellow region) meets the threshold ($>0.02 \mu\text{m}^2$). (E-left) the related domains which connect with each other but the overlapping area does not meet the threshold (E-middle), and the independent domains which have no association with each other (E-right). (F) Histogram of three types of domains from ten cells in three independent experiments. Scale bars are $5 \mu\text{m}$ in A–C. Scale bars are 200 nm in D and E.

Cite this: DOI: 10.1039/c0xx00000x

www.rsc.org/xxxxxx

ARTICLE TYPE

membrane. The first peak of the apical membrane (black column) represents the relative small clusters, similar to most clusters on the basal membranes (Figure 2G-left, inset in purple), while the second peak shows typical larger clusters on the apical membrane (Figure 2G-left, inset in blue). Additionally, the average circularity of cluster on the apical membrane is 0.41 ± 0.21 , which is approximately 1.56 times larger than that on the basal membrane, i.e. 0.27 ± 0.14 (Figure 2G-right, inset in purple). It is noted that the larger circularities (>0.5) means the cluster tend to form circular shape (Figure 2G-right, inset in blue). Furthermore, with assigning cell membrane as three areas, the histogram of densities of cluster per μm^2 of various cell areas (Figure 2H) also confirms the characteristic distribution of various clusters on the apical and basal membranes (as mentioned above). Considering the functions of N-GlcNAc-linked membrane proteins, such as cellular recognition, molecule trafficking, cell adhesion and migration, we presume that this distribution feature might promote the glycoconjugates to participate in the related physiological processes. Additionally, it is possible that such dramatic difference in distribution patterns of N-GlcNAcs on the apical and basal membranes are related to the polarized sorting in epithelial cells.³⁷

As previous studies confirmed that lipid rafts as membrane microdomains consist of specific membrane proteins and thereby

provide a hub for cellular signalling and protein trafficking,³⁸ we speculate that the aggregation of N-GlcNAcs in cluster as their functional domain is related to lipid raft domain. Additionally, Howard A. Stone *et al.*³⁹ found that the Glycans network can affect the phase behaviour of lipid membranes, revealing there is close relationship between the glycan clusters and lipid rafts. To prove this hypothesis, we implemented the dual color dSTORM imaging to locate N-GlcNAcs (Figure 3A) and lipid rafts (Figure 3B) on the Vero apical membrane. From the superimposed Figure 3C, a majority of N-GlcNAc clusters are colocalized with lipid rafts (Figure 3C). The magnified image (Figure 3D-left) clearly displays the representative colocalization (yellow color), which is further confirmed by the intensity profiles of these images (Figure 3D-middle). The positional relationships are sorted into three types according to their overlapped area, that is, the colocalized clusters (the colocalized area is larger than $0.02 \mu\text{m}^2$, Figure 3E-left), the related clusters (linking with each other but colocalized area is smaller than $0.02 \mu\text{m}^2$, Figure 3E-left), and the independent clusters (no overlapping, Figure 3E-right). From Figure 3F, the percentage of colocalized plus related clusters (68.8% for N-GlcNAc cluster (red columns), and 92.8% for lipid rafts (green columns) were quite high, which indicates that the formation of most N-GlcNAc clusters depends on or at least is related to lipid rafts.

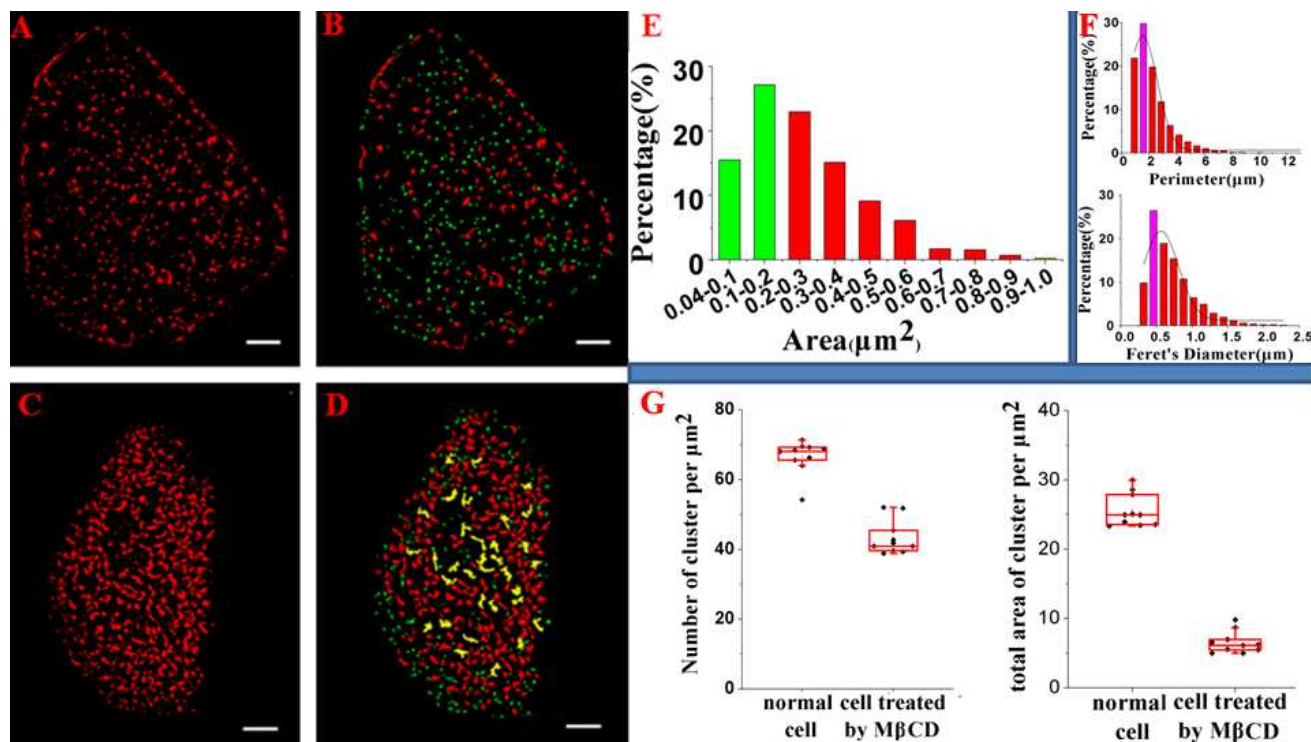


Fig. 4. The changed morphology of N-GlcNAc clusters after the treatment of methyl-β cyclodextrin (MβCD) on Vero cells. dSTORM images of N-GlcNAcs on representative apical membranes treated with MβCD (A) and normal apical surface (C). (B and D) dSTORM images of N-GlcNAcs with marking the clusters by different colors as Fig.2C. (E) Histograms of cluster areas (E), perimeters (F-up) and Feret's diameters (F-below) from 2891 qualified clusters of ten cells in three independent experiments. (G) The density of the clusters on the normal and MβCD-treated apical membranes. Scale bars are 5 μm in A–D.

Cite this: DOI: 10.1039/c0xx00000x

www.rsc.org/xxxxxx

ARTICLE TYPE

As lipid rafts are enriched with cholesterol and many functional proteins, with the extraction of cholesterol by methyl- β -cyclodextrin (M β CD) treatment, the integrity of lipid rafts are disrupted.^{40, 41} Therefore, to further verify the colocalization between N-GlcNAc clusters and lipid rafts, we imaged the N-GlcNAcs on the Vero apical membrane treated with M β CD. Compared with the corresponding images of N-GlcNAcs on the normal Vero apical surface (Figure 4C, D), the representative dSTORM image (Figure 4A) and the reassembled graph with all qualified clusters (Figure 4B) illustrate that there are dramatic changes with the destruction of lipid rafts, including the cluster area size and shape. After M β CD treatment, clusters become smaller, with 65.5% of them ranging from 0.04 to 0.3 μm^2 , in comparison with only 33% of clusters (0.04-0.45 μm^2) on the normal apical membrane (Figure 4E). Meanwhile, the average cluster perimeter ($1.52 \pm 0.07 \mu\text{m}$) and Feret's diameter ($0.56 \pm 0.03 \mu\text{m}$) largely decrease (Figure 4F), compared with those on the normal membrane ($4.26 \pm 0.16 \mu\text{m}$ and $1.24 \pm 0.04 \mu\text{m}$), for the density of cluster (Figure 4G), the number of clusters per unit membrane area reduces from 66.6% to 43.35%, and the total area of clusters per unit membrane area decreases from 25.6% to 6.54%, suggesting that the N-GlcNAc clusters are distributed more sparsely with the disruption of lipid rafts. These morphological changes confirm that the formation of most N-GlcNAc clusters is dependent on lipid rafts, indicating that there are a large number of N-GlcNAc-related glycoconjugates distributed in lipid rafts.

Conclusions

In summary, we performed dSTORM imaging combined with statistical analysis to reveal that a majority of N-GlcNAcs are aggregated in various micro-clusters on the Vero apical membrane. There is a significant difference in the distributions of N-GlcNAcs between the apical and basal membranes. Furthermore, the colocalization between the most N-GlcNAc clusters and lipid rafts suggests that the carbohydrate clusters just as lipid rafts are the functional aggregations of glycoproteins and glycolipids. With the ability of dSTORM imaging to localize saccharides in their biological environment at the molecular level, a comprehensive view of the distributions of all saccharides on the plasma membrane will be realized with more efforts. Importantly, comparing the nanometer-scale distributions of glycocalyx on cancer cells with that on normal cells, the alteration in expression and distribution pattern will promote to identify molecular markers for cancer diagnostics.

Acknowledgment

This work was supported by MOST (grant no. 2011CB933600), NSFC (Grant no. 21373200 and 31330082). We thank Institute of Immunology (the First Bethune Hospital Academy of Translational Medicine, Jilin University) for the instrument

support.

Notes and references

- ^a State Key Laboratory of Electroanalytical Chemistry, Changchun Institute of Applied Chemistry, Chinese Academy of Sciences, Changchun, Jilin 130022, P.R. China.
- ^b University of Chinese Academy of Sciences, Beijing 100049, P.R. China.
- ^c School of Chemistry and Chemical Engineering, University of Chinese Academy of Sciences, Beijing 100049, China
- † Electronic Supplementary Information (ESI) available: [details of any supplementary information available should be included here]. See DOI:10.1039/b000000x/
1. B. K. Brandley and R. L. Schnaar, *Leukocyte Biol.*, 1986, **40**, 97-111.
2. P. R. Crocker and T. Feizi, *Curr. Opin. Neurobiol.*, 1996, **6**, 679-691.
3. A. E. Smith and A. Helenius, *Science*, 2004, **304**, 237-242.
4. E. Gorelik, U. Galili and A. Raz, *Cancer Metast. Rev.s*, 2001, **20**, 245-277.
5. K. Ohtsubo and J. D. Marth, *Cell*, 2006, **126**, 855-867.
6. M. Herrmann, C. W. von der Lieth, P. Stehling, W. Reutter and M. Pawlita, *J. Virol.*, 1997, **71**, 5922-5931.
7. K. T. Pilobello and L. K. Mahal, *Curr Opin Chem Biol.*, 2007, **11**, 300-305.
8. K. Sugawara, T. Takayanagi, N. Kamiya, G. Hirabayashi and H. Kuramitz, *Talanta*, 2007, **71**, 1637-1641.
9. E. A. Smith, W. D. Thomas, L. L. Kiessling and R. M. Corn, *J. Am. Chem. Soc.*, 2003, **125**, 6140-6148.
10. O. Rusin, V. Král, J. O. Escobedo and R. M. Strongin, *Org. Lett.*, 2004, **6**, 1373-1376.
11. J. Screen, E. C. Stanca - Kaposta, D. P. Gamblin, B. Liu, N. A. Macleod, L. C. Snoek, B. G. Davis and J. P. Simons, *Angew. Chem.*, 2007, **119**, 3718-3722.
12. D. F. Smith and R. D. Cummings, *Mol. Cell. Proteomics*, 2013, **12**, 902-912.
13. J. Gao, L. Ma, D. Liu and Z. Wang, *Comb. Chem. High T, Scr.*, 2012, **15**, 90-99.
14. P. V. Chang, J. A. Prescher, M. J. Hangauer and C. R. Bertozzi, *J. Am. Chem. Soc.*, 2007, **129**, 8400-8401.
15. S. Stairs, A. A. Neves, H. Stöckmann, Y. A. Wainman, H. Ireland - Zecchini, K. M. Brindle and F. J. Leeper, *ChemBioChem*, 2013, **14**, 1063-1067.
16. B. Chen, Luke A. Gilbert, Beth A. Cimini, J. Schnitzbauer, W. Zhang, G.-W. Li, J. Park, Elizabeth H. Blackburn, Jonathan S. Weissman, Lei S. Qi and B. Huang, *Cell*, **155**, 1479-1491.
17. A. S. Stender, K. Marchuk, C. Liu, S. Sander, M. W. Meyer, E. A. Smith, B. Neupane, G. Wang, J. Li, J.-X. Cheng, B. Huang and N. Fang, *Chem. Rev.*, 2013, **113**, 2469-2527.
18. Z. Tian and A. D. Li, *Accounts Chem. Res.*, 2012, **46**, 269-279.
19. E. Abbe, *Arch. Mikrosk. Anat.*, 1873, **9**, 413-418.
20. S. W. Hell and J. Wichmann, *Opt. Lett.*, 1994, **19**, 780-782.
21. C. Alonso, *Biomol. Tech.*, 2013, **24**, S4.
22. X. Zhuang, *Nat. Photonics*, 2009, **3**, 365.
23. M. J. Rust, M. Bates and X. Zhuang, *Nat. Methods*, 2006, **3**, 793-796.
24. D. M. Owen, C. Rentero, J. Rossy, A. Magenau, D. Williamson, M. Rodriguez and K. Gaus, *Biophotonics*, 2010, **3**, 446-454.
25. S. T. Hess, T. P. Girirajan and M. D. Mason, *Biophys. J.* 2006, **91**, 4258-4272.
26. E. Betzig, G. H. Patterson, R. Sougrat, O. W. Lindwasser, S. Olenych, J. S. Bonifacio, M. W. Davidson, J. Lippincott-Schwartz and H. F. Hess, *Science*, 2006, **313**, 1642-1645.
27. S. T. Hess, T. J. Gould, M. V. Gudheti, S. A. Maas, K. D. Mills and J. Zimmerberg, *Proc. Natl. Acad. Sci.*, 2007, **104**, 17370-17375.

-
28. J. Z. Wu, J. Gao, M. Qi, J. Z. Wang, M. J. Cai, S. H. Liu, X. Hao, J. G. Jiang and H. D. Wang, *Nanoscale*, 2013, **5**, 11582-11586.
29. S. van de Linde, A. Löschberger, T. Klein, M. Heidebreder, S. Wolter, M. Heilemann and M. Sauer, *Nat. Protoc.*, 2011, **6**, 991-1009.
- 5 30. M. Heilemann, S. van de Linde, M. Schüttpelz, R. Kasper, B. Seefeldt, A. Mukherjee, P. Tinnefeld and M. Sauer, *Angew. Chem. Int. Edit.*, 2008, **47**, 6172-6176.
31. S. Letschert, A. Göhler, C. Franke, N. Bertleff - Zieschang, E. Memmel, S. Doose, J. Seibel and M. Sauer, *Angew. Chem. Int. Edit.*,
10 2014, **53**, 10921-10924.
32. S. T. Laughlin and C. R. Bertozzi, *Proc. Natl. Acad. Sci.*, 2009, **106**, 12-17.
33. Y. Y. Zhao, M. Takahashi, J. G. Gu, E. Miyoshi, A. Matsumoto, S. Kitazume and N. Taniguchi, *Cancer Sci.*, 2008, **99**, 1304-1310.
- 15 34. Y. Tian and H. Zhang, *Proteomics*, 2013, **13**, 504-511.
35. R. Henriques, M. Lelek, E. F. Fornasiero, F. Valtorta, C. Zimmer and M. M. Mhlanga, *Nat. Methods*, 2010, **7**, 339-340.
36. M. D. Abràmoff, P. J. Magalhães and S. J. Ram, *Biophotonics Int.*, 2004, **11**, 36-42.
- 20 37. S. Schuck and K. Simons, *J. Cell Sci.*, 2004, **117**, 5955-5964.
38. D. Lingwood and K. Simons, *Science*, 2010, **327**, 46-50.
39. A. B. Subramaniam, G. Guidotti, V. N. Manoharan and H. A. Stone, *Nat. Mater.*, 2013, **12**, 128-133.
40. R. Zidovetzki and I. Levitan, *BBA-Biomembranes*, 2007, **1768**, 1311-
25 1324.
41. M. Hao, S. Mukherjee and F. R. Maxfield, *Proc. Natl. Acad. Sci.*, 2001, **98**, 13072-13077.